

Battery-Free Monitoring of Micron-Level Vibrations with Sub-Hertz Frequency Accuracy: Toward Robust and Accurate Industrial Sensing

Yuanhao Feng^{ID}, Member, IEEE, Donghui Dai^{ID}, Jinyang Huang^{ID}, Panlong Yang^{ID}, Senior Member, IEEE, Xiang-Yang Li^{ID}, Fellow, IEEE, Feiyu Han^{*}^{ID}, Member, IEEE, and Lei Yang^{*}^{ID}, Senior Member, IEEE

Abstract—Accurately monitoring micron-level vibrations with sub-hertz frequency estimation error is critical for early fault detection in industrial equipment. Existing solutions either rely on powered sensors or suffer from limited accuracy in passive operation, restricting scalability and long-term deployment. We present *Vibro-Stethos*, a fully battery-free sensing system that accurately captures micron-level vibrations with sub-hertz frequency estimation error. It employs a dual-junction field-effect transistor (JFET) analog frontend to convert vibration into impedance modulation and encodes this onto passive RFID backscatter. An embedded RFID chip enables selective tag activation and provides path-invariant reference amplitude normalization. A Graph Attention Network (GAT)-based model adaptively fuses features from spatially distributed tags, enabling robust fault classification under tag sparsity and placement variation. Extensive evaluation demonstrates that *Vibro-Stethos* achieves amplitude measurement errors within 2 μm , frequency estimation errors below 0.1 Hz, and vibration fault classification accuracy of 93.7%. Real-world deployments on transformers further confirm its diagnostic capability. *Vibro-Stethos* offers a practical, robust, and accurate battery-free solution for pervasive industrial vibration monitoring.

Index Terms—Battery-free sensing, RFID backscatter, Vibration Monitoring, Graph Attention Networks, Industrial Fault Diagnosis

I. INTRODUCTION

VIBRATION sensing is fundamental to predictive maintenance and fault diagnosis in industrial systems [1]. Particularly critical is the accurate detection of micron-level vibrations with sub-hertz frequency resolution, as such subtle signals often serve as early indicators of structural or mechanical faults [2]. Effective fault diagnosis further requires long-term, continuous vibration monitoring to capture early anomalies and degradation trends.

Yuanhao Feng is with the University of Electro-Communications, Chofu 182-8585, Japan. (E-mail: fyhace@mail.ustc.edu.cn).

Donghui Dai and Lei Yang are with the Department of Computer Science, The Hong Kong Polytechnic University, Hong Kong 999077, China (E-mail: donghui.dai@connect.polyu.hk and liveyang@polyu.edu.hk).

Jinyang Huang is with the School of Computer Science and Information Engineering, Hefei University of Technology, Hefei 230026, China (E-mail: hjy@hfut.edu.cn).

Feiyu Han and Panlong Yang are with the School of Computer Science, Nanjing University of Information Science and Technology, Nanjing 210044, China (E-mail: {fyhan,003829}@nuist.edu.cn).

Xiang-Yang Li is with the School of Computer Science and Technology, University of Science and Technology of China, Hefei 230026, China (E-mail: xiangyangli@ustc.edu.cn).

Corresponding authors*: Feiyu Han and Lei Yang.

Conventional methods typically rely on contact-based sensors such as piezoelectric accelerometers [3] and strain gauges [4], or on non-contact optical vibrometers like Laser Doppler Vibrometers (LDVs) [5]. While these techniques offer micron-level precision, they require extensive wiring, regular maintenance, and, in the case of optical systems, strict line-of-sight alignment [6]. Furthermore, most conventional approaches rely on powered electronics and analog-to-digital conversion [1], limiting scalability in battery-constrained deployments.

In contrast, RF-based techniques such as RFID backscatter [7], [8] and mmWave radar [9]–[11] simplify deployment by eliminating physical wiring. However, RFID systems typically offer only millimeter-level sensitivity due to limited impedance modulation depth, while mmWave systems, although more precise, suffer from limited penetration, high directionality, and multipath sensitivity—particularly in cluttered or metallic environments.

This reveals a critical gap: achieving robust, accurate, and scalable micron-level vibration sensing without relying on batteries, optical alignment, or complex infrastructure.

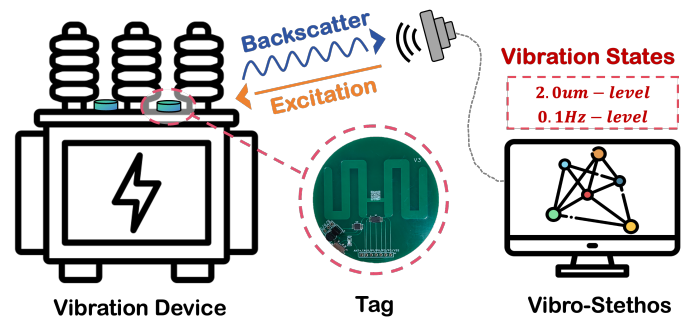


Fig. 1. Vibration monitoring with *Vibro-Stethos*: passive RFID tags integrated with dual-JFET and PZT sensors modulate micron-level vibrations onto backscatter signals for battery-free industrial monitoring and fault identification via GAT.

To bridge this gap, we present *Vibro-Stethos*, a fully battery-free vibration sensing system designed for long-term, scalable deployment in industrial settings. As illustrated in Fig. 1, the system uses surface-mounted passive tags to track structural vibrations at multiple points. Each tag operates without batteries and encodes vibration signals onto RF backscatter, which is

collected by a reader for real-time analysis. The data supports early fault detection—even under sparse, irregular, or dynamic tag layouts.

Implementing Vibro-Stethos requires addressing three key technical challenges:

- **Battery-Free Micron-Level Vibration Capture:** Existing vibration sensors rely on active amplification and digitization [1], making battery-free operation infeasible. Our prior single-JFET backscatter designs [12] further distort signal recovery by only modulating one polarity of vibration. **To address this**, we design a dual-JFET circuit with complementary P-JFET and N-JFET devices that enables full-wave impedance modulation and passive sensing of micron-level vibrations.
- **Tag-Level Control and Accurate Amplitude Recovery:** Co-located passive RFID tags can interfere with each other, and their signal amplitudes are affected by unknown path losses. **To solve this**, we use commercial RFID chips with EPC Gen2 support for selective activation, and introduce a path-invariant calibration method that differentially extracts vibration amplitude by referencing the tag’s own modulation.
- **Robust Fault Recognition under Tag Placement Variability:** Conventional classifiers assume fixed tag layouts, which limits robustness to tag loss or nonuniform deployment. **To address this**, we adopt a Graph Attention Network (GAT) that builds flexible tag graphs and learns attention weights to prioritize informative nodes, enabling reliable fault detection under deployment variability.

In summary, the contributions of this paper are threefold:

- We propose *Vibro-Stethos*, the first fully battery-free vibration sensing system that enables accurate, scalable monitoring of micron-level mechanical vibrations with sub-hertz frequency accuracy. The system requires neither batteries nor wiring, and supports long-term multi-point deployment in industrial environments.
- We design a complete sensing pipeline that integrates a dual-JFET-based passive sensor tag with a Graph Attention Network for adaptive fault classification. This joint hardware-software approach supports full-wave signal capture and robust anomaly recognition under sparse and variable tag placements.
- We validate *Vibro-Stethos* through controlled lab tests and real-world deployments on three types of industrial transformers. Compared to mmVib [11], our system reduces median amplitude error from 8% to 2%, and frequency error from 0.5% to below 0.1%—achieving 4× and 5× improvements, respectively. It further achieves 93.7% fault detection accuracy, even under irregular layouts and without active sensing hardware.

Together, these contributions establish *Vibro-Stethos* as a practical and accurate solution for pervasive industrial vibration monitoring. The remainder of the paper is organized as follows: Sec. II reviews related work in vibration sensing and fault diagnosis. Sec. III presents the battery-free analog tag design of *Vibro-Stethos*. Sec. IV details the signal processing pipeline and graph-based classification model. Sec. V eval-

uates the system’s accuracy and robustness under both lab and real-world conditions. Sec. VI discusses practical considerations, energy architecture, and design rationale. Finally, Sec. VII concludes the paper.

II. RELATED WORK

Vibration measurement has been studied extensively across a variety of sensing modalities, each with its tradeoffs in terms of accuracy, deployment complexity, and environmental constraints. We categorize related work into conventional methods and advanced wireless backscatter systems, followed by a review of fault detection models.

A. Conventional Vibration Sensing

Traditional approaches are dominated by contact-based transducers like piezoelectric ceramics (e.g., PZT) [3], [13], [14], MEMS accelerometers [15], [16], and strain gauges [4]. While offering high precision, they typically require wiring and an active power supply, complicating deployment on existing machinery. Non-contact methods such as Laser Doppler Vibrometry (LDV) [5], [6], [17] achieve exceptional micron-level accuracy but demand a stable line-of-sight, which is often impractical in industrial settings. Vision-based [18]–[20] and acoustic-based [21], [22] methods offer remote sensing but are constrained by lighting conditions and ambient noise, respectively. These limitations motivate the need for robust, passive, and wireless sensing solutions.

B. Advanced Wireless Backscatter Sensing Systems

Wireless RF sensing offers a compelling alternative. Standard UHF RFID systems have been widely adapted for sensing by exploiting backscatter amplitude or phase variations [7], [8], [23]–[26]. A significant advancement was demonstrated by Xie et al., achieving sub-millimeter accuracy by processing the phase of commodity RFID signals [27]. Other research has explored specialized hardware, such as the SAW RFID system by Caldero and Zoeke, which uses a multi-channel reader to monitor rotating shafts [28]. Concurrently, a parallel line of research on analog backscatter has pushed sensitivity to new limits for different applications. Systems like **RF Bandaid** [29] and **MARS** [30] leverage Frequency Modulation (FM) to achieve high-fidelity sensing for wearables and human-computer interaction (HCI). Other RF modalities have also been explored, including WiFi CSI-based approaches [31]–[33] and mmWave radar systems [9]–[11], [34], [35]. While WiFi-based methods are often limited by low sampling rates, mmWave systems like mmVib [9] offer high precision but at the cost of active power and expensive hardware.

While these advanced backscatter systems showcase impressive capabilities, they are optimized for domains other than industrial diagnostics. In contrast, *Vibro-Stethos* introduces an end-to-end system specifically architected for the unique demands of high-precision industrial monitoring. Our novelty lies in a hardware-software co-design that combines a new analog front-end—using a dual-JFET pair to directly transduce

TABLE I
COMPARISON OF VIBRO-STETHOS WITH ADVANCED WIRELESS SENSING SYSTEMS.

System	Core Tech.	Application	Mechanism	Key Goal	Multi-Tag Scheme
Commodity RFID [27]	UHF RFID	General Sensing	Phase Shift	Sub-mm Accuracy	Standard Protocol
SAW RFID [28]	SAW RFID	Rotating Machinery	Power/Phase Mod.	Wideband Spectrum	Multi-channel HW
Analog FM [29], [30]	Analog Circuit	Wearables / HCI	R/C → FM	nW/μW Power	FDM
RF-parrot [24]	UHF RFID	Acoustic Eavesdropping	Vibration Mod.	Audio Fidelity	Not Specified
mmVib [9]	mmWave Radar	Vibration Sensing	Radar Phase	Micron Accuracy	Beamforming
Vibro-Stethos	UHF RFID + Analog FE	Industrial Diagnosis	Voltage → AM	Micron/Sub-Hz Acc.	Polling + GAT SW

a PZT's voltage into a strong amplitude modulation—with a GAT-based software model. This integrated approach allows us to achieve and rigorously validate a new tier of quantitative precision (micron-level, sub-hertz) essential for detecting incipient faults. Furthermore, by building upon the standard EPC Gen2 RFID protocol, our system inherently supports scalable multi-tag deployment, enabling the GAT to robustly analyze the complex spatial vibration patterns found on large industrial equipment. A summary of this comparison across key technical dimensions is presented in Table I.

C. Vibration-Based Fault Detection Models

Recent years have seen a growing interest in data-driven fault classification models based on vibration signatures [36]–[39]. Traditional methods rely on frequency-domain features [40] followed by thresholding or PCA-based classifiers. While effective in fixed settings, these methods struggle under layout variability. Deep learning approaches, such as CNNs [41], have improved classification accuracy but often assume fixed tag positions. Our work introduces a graph attention network (GAT) [42] that adaptively weighs tag contributions based on spatial and spectral relevance, enabling robust multi-tag fusion under arbitrary deployment.

III. BATTERY-FREE ANALOG TAG DESIGN FOR VIBRATION SENSING

This section presents the hardware design of the Vibro-Stethos tag, which enables battery-free vibration sensing through analog signal modulation. We first describe the overall architecture and key components of the tag in Sec. III-A. Then, Sec. III-B develops a circuit-level model that explains how mechanical vibrations are converted into impedance variations. Sec. III-C analyzes the limitations of single-JFET designs and introduces a dual-JFET configuration for full-cycle signal conversion. Finally, Sec. III-D details how the RFID module enables tag-level identification, control, and signal path calibration.

A. Overall Architecture and Operating Principle

Fig. 2 illustrates the architecture of the Vibro-Stethos tag, which consists of four key modules: a piezoelectric transducer (PZT), a dual-JFET analog modulator, a commercial RFID

chip, and an antenna with an impedance matching network. These modules work together to convert mechanical vibrations into impedance-modulated backscatter signals, enabling passive vibration sensing without any onboard power supply.

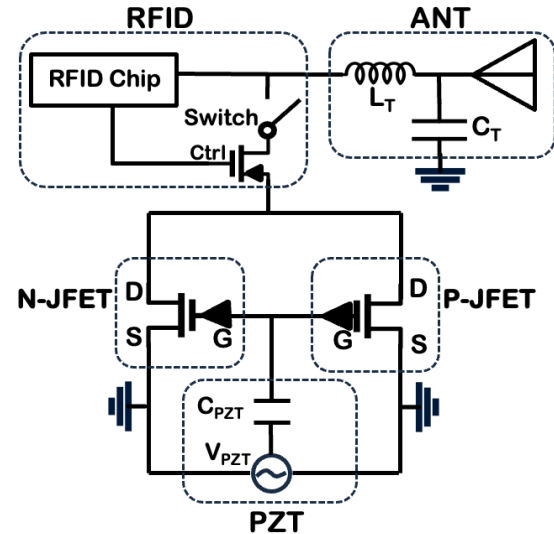


Fig. 2. Overall circuit architecture of the Vibro-Stethos tag. The system integrates a piezoelectric transducer (PZT), a dual-JFET analog modulator, an RFID chip with ID and control capability, and an antenna with an L-C matching network for impedance-modulated backscatter transmission.

PZT Module: The PZT acts as a mechanical-to-electrical transducer, modeled as a voltage source V_{PZT} in series with a capacitor C_{PZT} . Mechanical stress induces a voltage across the PZT terminals, which is proportional to the vibration amplitude and frequency. This voltage serves as the input signal to the analog modulation circuit. In typical industrial scenarios, vibration amplitudes range from tens to several hundred micrometers, corresponding to PZT output voltages in the range of 10–1000 mV depending on mounting stiffness and frequency.

JFET Modulation Module: Two complementary JFETs—a P-channel and an N-channel device—are used to convert the PZT voltage into resistance modulation. In the ohmic region [43], the drain-source (D-S) resistance of each JFET varies non-linearly with gate-source (G-S) voltage V_{GS} . The complementary configuration enables full-cycle response, as

detailed in Sec. III-C. In our design, a V_{GS} swing as small as 30–200 mV is sufficient to induce noticeable resistance change, enabling effective analog modulation even under low-amplitude vibration.

Antenna and Matching Network: An L-C matching network interfaces the JFETs to the antenna, ensuring impedance compatibility. Changes in drain-source resistance directly affect the antenna's load impedance, thereby modulating the amplitude of the backscattered RF signal.

RFID Module: We use the EM4325 chip [44], which follows the EPC Gen2 standard and provides each tag with a unique identifier. An integrated RF switch connects or disconnects the JFETs from the antenna based on reader commands. This allows the reader to selectively activate tags and isolate their vibration-modulated signals from the background.

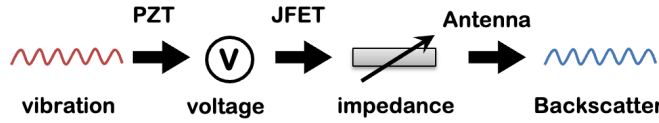


Fig. 3. Signal conversion process from vibration to backscatter. Mechanical stress generates a voltage from the PZT, which modulates the gate-source voltage of the JFETs. This alters the antenna load impedance and encodes vibration information into the amplitude of the backscattered RF signal.

Together, these four modules enable the Vibro-Stethos tag to convert mechanical vibrations into uniquely identifiable, amplitude-modulated backscatter signals. As illustrated in Fig. 3, when the PZT senses vibration-induced stress, it generates a small voltage that modulates the gate-source voltage of the JFETs, resulting in changes in load impedance seen by the antenna. The antenna reflects an RF signal whose amplitude varies with the mechanical vibration. The RFID chip selectively activates the tag and provides a reference signal for amplitude calibration.

B. From Mechanical Vibrations to Backscatter Signal with Single JFET

To understand how mechanical vibrations are modulated into RF backscatter, we begin with the basic sensing circuit shown in Fig. 4, which consists of a PZT, a single P-channel JFET, and an RFID antenna interface.

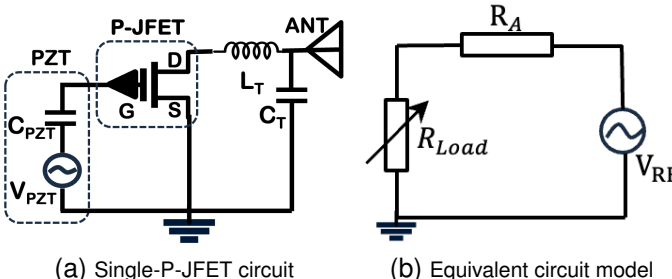


Fig. 4. (a) Simplified sensing circuit using a single P-JFET connected to a PZT and an antenna; (b) Equivalent model where vibration-induced voltage modulates JFET resistance, altering antenna load impedance and backscatter amplitude.

Voltage Generation from Vibration: The sensor used to capture mechanical vibrations is a low-cost, 5 cm diameter

piezoelectric transducer (PZT), shown in Fig. 5(a). This component, commonly available as a buzzer element, consists of a central piezoelectric ceramic disc bonded to a metal plate. It operates on the direct piezoelectric effect: when subjected to mechanical stress from a vibrating surface, the ceramic generates a charge proportional to the strain. This results in a time-varying gate-source voltage V_{GS} for the JFET, which can be modeled as:

$$V_{GS} = \frac{d_{33}}{C_{PZT}} A_v \sin(2\pi f_v t) \quad (1)$$

where A_v and f_v denote the vibration amplitude and frequency, d_{33} is the piezoelectric coefficient, and C_{PZT} is the sensor's effective capacitance.

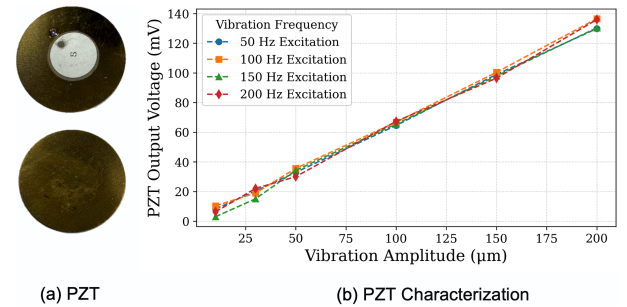


Fig. 5. (a) The piezoelectric transducer (PZT) used in our system, showing the front (ceramic disc) and back (metal plate) of the 5 cm diameter buzzer element. (b) Experimental characterization of the PZT sensor, demonstrating a highly linear voltage-amplitude response whose mapping coefficient is largely independent of frequency in the 50–200 Hz range.

While Eq. (1) provides the theoretical foundation, the effective mapping coefficient in practice is also influenced by mounting conditions. Therefore, we empirically characterized the sensor's response using a high-precision laser Doppler vibrometer (LDV) as a ground-truth reference. The results, presented in Fig. 5(b), yield two critical insights. First, the PZT's voltage output exhibits a highly linear relationship with vibration amplitude across all tested frequencies. Second, the slopes of these lines are nearly identical in the 50–200 Hz range, which is typical for industrial machinery. These findings confirm that the voltage-to-vibration mapping is not only stable but also robustly independent of frequency in this operational range, providing a solid basis for the universal, one-time calibration procedure detailed in Sec. V-A.

Resistance Modulation via JFET: In the ohmic region [43], the P-JFET's drain-source resistance R_P varies nonlinearly with V_{GS} due to modulation of the channel depletion width. This relation can be modeled as:

$$R_P = \frac{R_{P,\text{on}}}{1 - \frac{V_{GS}}{V_{P,\text{off}}}} \quad (2)$$

where $R_{P,\text{on}}$ is the resistance when $V_{GS} = 0$ and $V_{P,\text{off}} > 0$ is the cutoff voltage.

The structural behavior and resistance characteristics of the P-JFET (2SJ103) are illustrated in Fig. 6. Panel (a) shows a cross-sectional view of the device, where the gate-controlled depletion width modulates the conduction channel. Panel (b) plots the theoretical relationship between R_P and V_{GS} , confirming the nonlinearity described in Eq. (2).

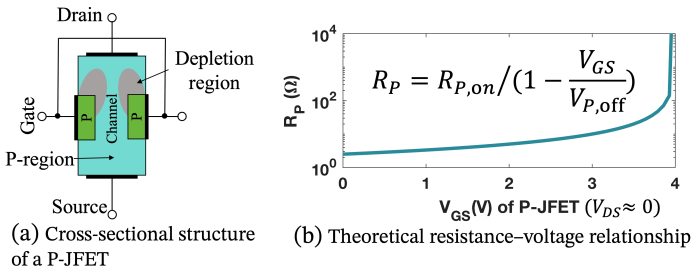


Fig. 6. (a) Cross-sectional view of a P-channel JFET (2SJ103) showing gate-controlled depletion width; (b) Theoretical R_P - V_{GS} curve based on Eq. (2), illustrating nonlinear resistance growth near cutoff.

Antenna Load Modulation: The varying resistance R_P is converted into antenna-visible impedance via an L-C matching network, which acts as a step-up transformer:

$$R_{\text{Load}} = \frac{\omega^2 L_T^2}{R_P} = \frac{\omega^2 L_T^2}{R_{P,\text{on}}} \left(1 - \frac{V_{GS}}{V_{P,\text{off}}} \right) \quad (3)$$

This impedance appears in series with the antenna resistance R_A , forming the total load seen by the reader.

Backscatter Amplitude Modulation: According to standard RFID theory [45], the reflected amplitude is given by:

$$A_{\text{back_vib}} = \frac{K}{R_A + R_{\text{Load}}} \quad (4)$$

where K depends on reader power, path loss, and antenna gain. Substituting Eq. (3) and linearizing under the small-signal assumption $V_{GS} \ll V_{P,\text{off}}$ (e.g., $V_{GS} < 200$ mV and $V_{P,\text{off}} \approx 3\text{--}4$ V), we derive:

$$A_{\text{back_vib}} \approx K \left(\frac{1}{R_A + R_L} + \frac{R_L}{(R_A + R_L)^2} \cdot \frac{V_{GS}}{V_{P,\text{off}}} \right) \quad (5)$$

$$= K(a_0 + a_1 \cdot V_{GS}) \quad (6)$$

where $R_L = \omega^2 L_T^2 / R_{P,\text{on}}$, and the constants a_0 and a_1 are defined as:

$$a_0 = \frac{1}{R_A + R_L}, \quad a_1 = \frac{R_L}{(R_A + R_L)^2 V_{P,\text{off}}}$$

This analysis confirms that mechanical vibrations induce sinusoidal variations in backscatter amplitude. However, due to the unipolar nature of the JFET, only one polarity of the vibration signal is captured, resulting in half-wave modulation and limited signal fidelity. This motivates the dual-JFET design discussed in Sec. III-C.

C. Full-Wave Signal Restoration via Dual-JFET Design

The single-JFET circuit described earlier captures only one polarity of the vibration signal, due to the unipolar conduction characteristics of the JFET. As shown in Fig. 7(a), the ground-truth signal from the PZT exhibits a clean sinusoidal waveform at 50 Hz. However, the backscatter signal from a P-JFET-based tag captures only the positive half-cycles, resulting in clipped waveforms and distorted amplitude recovery, as demonstrated in Fig. 7(b).

To overcome this limitation, we propose a dual-JFET design that combines a P-JFET and an N-JFET in parallel. Each device modulates a different polarity of the vibration signal:

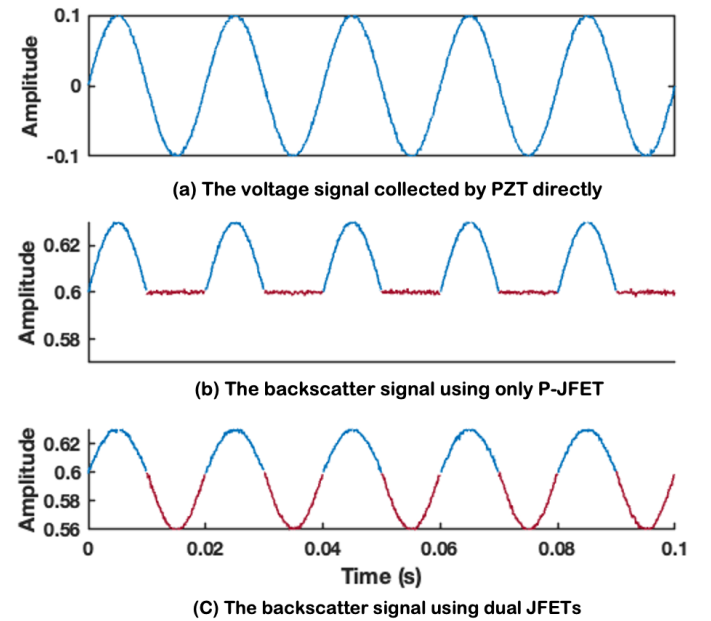


Fig. 7. Backscatter waveform comparison under a 50 Hz vibration source. (a) Ground-truth voltage measured directly from the PZT sensor, showing a full sinusoidal waveform. (b) Backscatter signal captured from a single P-JFET tag, exhibiting a clipped half-cycle response due to unipolar resistance modulation. (c) Backscatter signal from the proposed dual-JFET design, demonstrating full-wave restoration and accurate signal reconstruction.

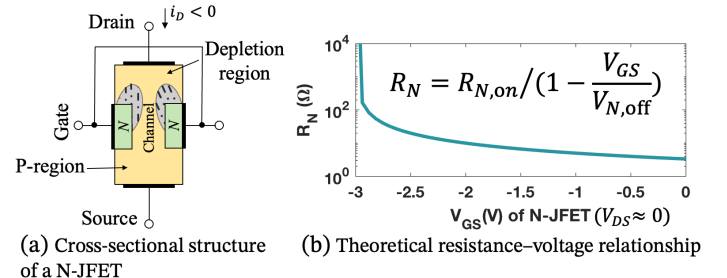


Fig. 8. (a) Cross-sectional structure of an N-channel JFET (2SK246), where negative gate-source voltage expands the depletion region and modulates channel conductivity. (b) Theoretical resistance-voltage relationship modeled by $R_N = R_{N,\text{on}} / (1 - \frac{V_{GS}}{V_{N,\text{off}}})$, showing decreasing resistance as V_{GS} becomes more negative. This behavior complements the P-JFET, enabling full-wave signal modulation.

the P-JFET responds to positive V_{GS} , and the N-JFET to negative V_{GS} . Fig. 8(a) shows the cross-sectional structure of the N-JFET, where negative gate-source voltage expands the depletion region and increases resistance. This behavior is modeled as:

$$R_N = \frac{R_{N,\text{on}}}{1 - \frac{V_{GS}}{V_{N,\text{off}}}} \quad (7)$$

where $R_{N,\text{on}}$ is the on-state resistance, and $V_{N,\text{off}} < 0$ is the pinch-off voltage. Fig. 8(b) illustrates this nonlinear relationship across the negative voltage range.

By feeding the same V_{GS} signal from the PZT to both devices, the dual-JFET configuration achieves continuous resistance modulation over the full sinusoidal cycle. This enables

full-wave signal encoding in the backscattered RF amplitude. The backscatter amplitude model in Eq. 5 is accordingly extended as:

$$A_{\text{back_vib}} = \begin{cases} K \left(\frac{1}{R_A+2R_L} + \frac{R_L}{R_A+2R_L} \cdot \frac{V_{GS}}{V_{N,\text{off}}} \right), & V_{GS} < 0 \\ K \left(\frac{1}{R_A+2R_L} + \frac{R_L}{R_A+2R_L} \cdot \frac{V_{GS}}{V_{P,\text{off}}} \right), & V_{GS} \geq 0 \end{cases} \quad (8)$$

We experimentally validate this design under identical vibration conditions. As shown in Fig. 7(c), the dual-JFET configuration restores the complete sinusoidal waveform, closely following the ground-truth PZT signal. This full-cycle response significantly improves amplitude estimation accuracy, especially in low-vibration regimes where half-wave distortion introduces large relative errors. The dual-JFET architecture thus forms the foundation of reliable, battery-free vibration sensing across real-world industrial scenarios.

D. RFID-Controlled Tag Selection and Path Calibration

In real-world deployments, vibration monitoring often requires multiple tags distributed across various surfaces or machine components. This introduces two critical challenges: First, it becomes difficult to control which tag is actively sensing at any given time, leading to signal collision and ambiguity in backscatter demodulation. Second, the amplitude of the received backscatter signal depends not only on the vibration strength but also on tag-specific propagation factors such as antenna orientation, distance, and multipath effects. These variations manifest as an unknown path gain K , which must be compensated to ensure accurate amplitude recovery.

To address both issues, Vibro-Stethos incorporates a commercial RFID chip in each tag, which provides digital control and a built-in reference modulation signal. These capabilities enable selective tag activation and path-invariant calibration without additional hardware or tag-specific calibration effort.

Tag-Level Selective Activation: We adopt the EM4325 RFID chip, compliant with the EPC Gen2 standard, which allows each tag to respond to reader-issued queries using its unique 96-bit identifier. Through the standard Select command, the reader can address individual tags or groups, thereby preventing collision and enabling scalable multi-tag operation. As shown in Fig. 2, the RFID chip is connected to an RF switch that controls the connection between the antenna and the dual-JFET analog modulation module. When the sensing function is disabled, the RF switch isolates the JFETs from the antenna, ensuring that no vibration-induced modulation occurs. This mechanism guarantees that only the selected tag contributes to the backscatter signal at any given time.

Path-invariant Normalization Using Embedded RFID Signal. While vibration frequency estimation is generally insensitive to channel gain, accurate amplitude recovery requires compensating for the unknown, tag-specific propagation gain K . To provide an intuitive understanding of this mechanism, Fig. 9 illustrates how both the vibration-induced analog signal and the digital ON/OFF keying reference traverse the same antenna path and therefore experience identical propagation effects.

During normalization, the reader alternates the tag between ON and OFF states, producing a measurable amplitude difference in the backscattered signal, defined as $\Delta A_{\text{RFID}} = A_{\text{ON}} - A_{\text{OFF}}$. This reference is then used to normalize the vibration-induced amplitude, effectively eliminating the unknown gain factor K . The corresponding signal processing is formalized in Sec. IV-A.

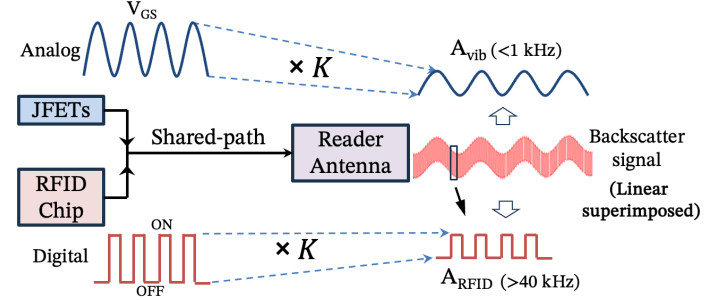


Fig. 9. Illustration of **path-invariant normalization**. Both the analog vibration-induced signal (top) and the digital ON/OFF keying signal (bottom) are modulated through the same antenna path and experience identical propagation gain K , so their ratio cancels out K , enabling robust amplitude normalization.

IV. GAT-BASED VIBRATION FAULT DETECTION

This section outlines the pipeline used by *Vibro-Stethos* to infer fault states from vibration-induced amplitude modulation backscatter signals. From each tag's RF response, we extract the dominant vibration frequency f_v and calibrated amplitude A_{vib} , which jointly characterize structural vibration behavior. To handle sparse and variable tag layouts, we construct a spatial graph and apply a Graph Attention Network (GAT) to adaptively fuse multi-tag features. The complete pipeline is detailed in the subsections below.

A. Backscatter Signal Processing

The backscatter signal received from each tag encodes vibration-induced amplitude modulation superimposed on its EPC Gen2 response. Fig. 10 shows a representative signal in both time and frequency domains. In the time domain, vibration appears as a low-frequency envelope on top of the reader-initiated tag response. Applying an FFT to this envelope reveals a dominant frequency peak (e.g., 200 Hz) and its harmonics, confirming that both vibration frequency and strength can be reliably extracted.

We aim to extract two critical features from the backscatter signal: (i) the dominant vibration frequency f_v , and (ii) the corresponding normalized amplitude A_{vib} , which together serve as robust input for fault classification.

Frequency Estimation via Spectral Analysis: The time-domain signal is segmented into 10 s windows, each multiplied by a Hann window function to suppress spectral leakage. We then apply the Fast Fourier Transform (FFT) and locate the peak in the power spectral density (PSD) to estimate the vibration frequency f_v . This frequency directly reflects the physical oscillation of the vibrating surface. In our experiments, healthy

machine states typically exhibit stable resonance frequencies (e.g., 50 Hz or 100 Hz), whereas deviations suggest structural imbalance or loosened components.

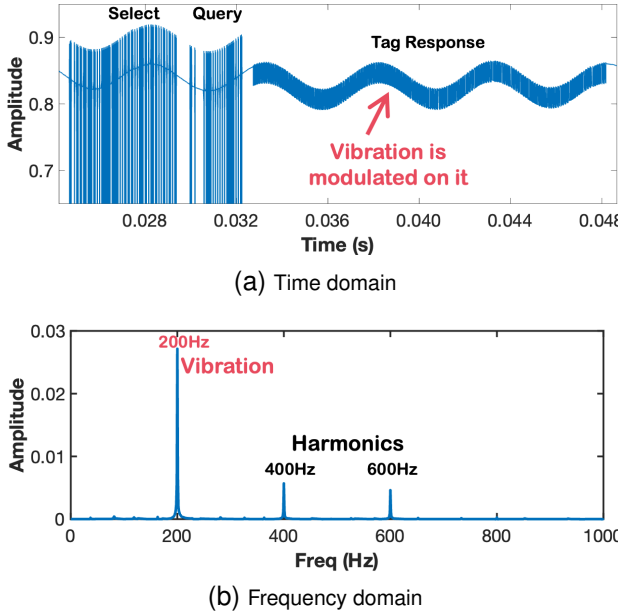


Fig. 10. Backscatter signal observed in the time and frequency domains. (a) Time-domain signal showing the EPC Gen2 protocol phases: *Select*, *Query*, and the *Tag Response*, where vibration-induced amplitude modulation is embedded. (b) Frequency-domain spectrum of the tag response, with a dominant peak at 200 Hz and visible harmonics at 400 Hz and 600 Hz, revealing the periodic nature of the mechanical vibration.

Amplitude Estimation via Path-Invariant Normalization: As derived previously in Eq. (6), the vibration-induced backscatter amplitude is linearly related to the gate-source voltage V_{GS} , but scaled by an unknown path gain K . This makes absolute amplitude recovery nontrivial, as K depends on reader transmission power, antenna alignment, and multipath fading—factors that vary across space and deployment conditions.

To eliminate this path-dependent scaling, we exploit the co-located RFID chip's built-in ON/OFF keying modulation as a differential reference. As described in Sec. III-D and illustrated in Fig. 9, both the analog vibration signal and the digital RFID reference signal are reflected through the same antenna and traverse an identical RF path to the reader. This shared-path configuration ensures that both signals experience the same propagation gain K , enabling path-invariant amplitude normalization.

Formally, the backscatter amplitude modulated by the RFID chip can be expressed as:

$$A_{\text{back_RFID}} = K \cdot (b_0 + b_1 \cdot V_{\text{RFID}}), \quad V_{\text{RFID}} = \begin{cases} 1, & \text{ON} \\ 0, & \text{OFF} \end{cases} \quad (9)$$

where b_0 and b_1 are constants related to the antenna and RFID impedance. Taking the amplitude difference between ON and OFF states yields a path-invariant reference:

$$\Delta A_{\text{RFID}} = A_{\text{back_RFID}}^{\text{ON}} - A_{\text{back_RFID}}^{\text{OFF}} = K \cdot b_1 \quad (10)$$

Notably, the RFID modulation frequency (typically 40–160 kHz) is orders of magnitude higher than the vi-

bration frequency (≤ 1 kHz). Therefore, the vibration-induced change in backscatter amplitude between the ON and OFF states—measured over adjacent microsecond-scale samples—can be safely assumed negligible. This ensures that the difference ΔA_{RFID} reflects only the effect of RFID state change, and not mechanical vibration.

Similarly, the vibration-induced backscatter amplitude changes from its idle baseline as:

$$\Delta A_{\text{vib}} = A_{\text{back_vib}}^{V_{GS}} - A_{\text{back_vib}}^{V_{GS}=0} = K \cdot a_1 \cdot V_{GS} \quad (11)$$

Taking the ratio of these two differential measurements eliminates K , yielding:

$$\frac{\Delta A_{\text{vib}}}{\Delta A_{\text{RFID}}} = \frac{a_1}{b_1} \cdot V_{GS} \quad (12)$$

This ratio provides a linear, path-invariant mapping from the backscatter signal to the gate-source voltage V_{GS} , which is in turn proportional to the vibration amplitude via the PZT's electrical response (as derived in Eq. (8)). All quantities on the left-hand side can be directly extracted from the measured waveform, enabling robust and environment-independent amplitude estimation.

B. Graph-Based Fault Recognition Model

Faults in industrial equipment, such as transformers, manifest as changes in vibration amplitude and frequency. To detect such anomalies, we deploy multiple RFID tags across the surface of the equipment. These tags provide spatially distributed sensing without the need for fixed placements or wired infrastructure.

Traditional classifiers, such as CNNs, assume fixed sensor topologies and therefore cannot adapt to deployment variability or structural changes. To address this limitation, we adopt a graph-based learning framework that models the vibration propagation structure using a node-edge graph. This approach supports robust fault recognition under dynamic tag configurations.

Each transformer is abstracted as a graph $G = (V, E)$, where the node set V includes RFID tags and conceptual vibration sources (e.g., internal windings). Although vibration sources are not directly observable, their effects are captured through the responses of surrounding tags. Each tag node $v_i \in V$ is connected to its spatial neighbors and at least one nearby vibration source. Fig. 11(a) illustrates this representation, with circular nodes representing tags and triangular nodes representing sources. Fig. 11(b) shows the corresponding binary adjacency matrix.

Graph Structure Definition: We define an undirected graph $G = (V, E)$, where each node corresponds to either a sensing tag or a vibration source. An initial binary adjacency matrix $\mathbf{A} \in \{0, 1\}^{n \times n}$ is constructed such that $A_{ij} = 1$ if tag i is connected to tag j , or either is connected to a vibration source. We then apply exponential distance-based weighting:

$$A'_{ij} = \exp(-\delta_0 \cdot d_{ij}) \cdot A_{ij} \quad (13)$$

where d_{ij} is the Euclidean distance between nodes and δ_0 is a damping coefficient reflecting material attenuation. This step

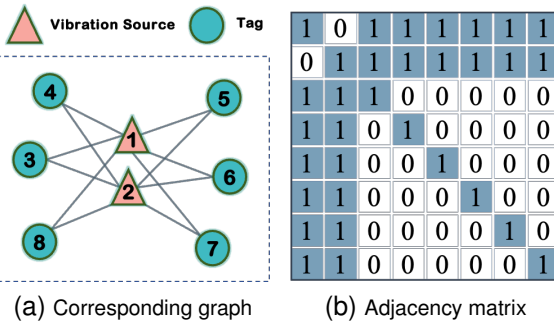


Fig. 11. (a) Constructed vibration graph, where circular nodes are Vibro-Stethos tags and triangular nodes denote vibration sources. Edges represent spatial connectivity. (b) Corresponding binary adjacency matrix A before Gaussian weighting, which is applied to yield the final weighted graph A' .

promotes localized feature propagation and suppresses long-range noise.

Node Feature Representation: The feature representation for the graph is constructed in three steps: single-tag feature extraction, justification of temporal synchronization, and aggregation.

First, each tag i in the graph collects a 10-second segment of the backscattered signal. We apply a Fast Fourier Transform (FFT) to this segment to extract its vibration spectrum over a frequency range of 1–500 Hz. With a 0.1 Hz resolution, this process yields a 4991-dimensional feature vector $\mathbf{H}_i \in \mathbb{R}^{4991}$ that represents the tag's local vibration signature.

Next, to construct a complete graph, these feature vectors are gathered by polling the tags sequentially. For our primary application of monitoring large power transformers, prior work [38] has shown that their vibration states are highly stable over several minutes. Given that our system collects a 10-second data segment from each tag, constructing a graph from a typical set of five tags takes approximately 50 seconds. This data acquisition period is significantly shorter than the multi-minute stability window of the transformer. This temporal stability, therefore, permits the features from different tags to be treated as effectively synchronized. The limitations of this approach for equipment with more transient vibrations are discussed in Sec. VI.

Finally, all individual feature vectors from the n tag nodes in the graph are aggregated to form the final feature matrix $\mathbf{H} \in \mathbb{R}^{4991 \times n}$, which serves as the input to our classification model.

Graph Labels and Learning Objective: Each vibration graph corresponds to one of $C = 7$ labeled operating states, comprising one normal condition and six transformer fault types (e.g., winding short, clamp looseness) [37]. The classification model is trained to map the node features and graph structure to these categories.

During training, additional synthetic graphs are generated by sampling various tag subsets and layouts to enhance the model's generalization. Graph labels are assigned using two methods: (i) in lab settings, faults are simulated using speaker-emitted profiles; (ii) in field deployments, labels are confirmed by power system engineers based on excitation settings and sensor feedback.

Graph Convolutional Network (GCN): We implement a spectral GCN [46], where each layer updates node embeddings as:

$$\mathbf{H}^{(l+1)} = \sigma(\hat{\mathbf{A}}\mathbf{H}^{(l)}\mathbf{W}^{(l)}) \quad (14)$$

Here, $\hat{\mathbf{A}}$ is the normalized adjacency matrix with self-loops, $\mathbf{H}^{(l)}$ is the feature matrix at layer l , $\mathbf{W}^{(l)}$ is a trainable weight matrix, and σ is an activation function (e.g., ReLU). The final layer is pooled and passed to a softmax classifier to predict the fault type.

This GCN-based design allows effective aggregation of spatial and spectral information across the tag network, enabling accurate and layout-independent fault recognition. The following section describes an enhanced variant based on Graph Attention Networks (GAT) to further improve robustness.

C. Attention-Based Inference via GAT

GCNs provide a solid baseline but assign equal weight to all neighboring nodes during feature aggregation, limiting adaptability in real-world deployments where tag layouts may be sparse, irregular, or reconfigurable. To overcome this, we adopt a Graph Attention Network (GAT) that introduces a learnable attention mechanism, allowing each node to weigh its neighbors based on contextual relevance.

As shown in Fig. 12, the GAT model encodes tag-level vibration features into node embeddings, propagates them through attention-weighted layers, and outputs a graph-level fault classification.

GAT Formulation: For each node i , its updated representation \mathbf{h}'_i is computed as:

$$\mathbf{h}'_i = \sigma \left(\sum_{j \in \mathcal{N}(i)} \alpha_{ij} \cdot \mathbf{W}\mathbf{h}_j \right) \quad (15)$$

where \mathbf{W} is a shared weight matrix, $\sigma(\cdot)$ is a nonlinear activation function, and α_{ij} is the attention coefficient indicating the importance of node j to i . The coefficients are computed as:

$$\alpha_{ij} = \frac{\exp(\text{LeakyReLU}(\mathbf{a}^\top [\mathbf{W}\mathbf{h}_i \| \mathbf{W}\mathbf{h}_j]))}{\sum_{k \in \mathcal{N}(i)} \exp(\text{LeakyReLU}(\mathbf{a}^\top [\mathbf{W}\mathbf{h}_i \| \mathbf{W}\mathbf{h}_k]))} \quad (16)$$

where \mathbf{a} is a learnable weight vector and $\|$ denotes vector concatenation. This formulation allows the model to dynamically prioritize more informative neighbors.

Model Architecture and Training: We implement a multi-head GAT with $K = 4$ parallel attention heads, each computing independent attention maps and node embeddings. The outputs are concatenated to enhance representation diversity and stabilize training. The same node feature matrix \mathbf{H} and weighted adjacency matrix \mathbf{A}' used in the GCN baseline are reused. The model is trained end-to-end using cross-entropy loss over graph-level fault labels.

This attention mechanism improves both classification accuracy and resilience to tag sparsity and deployment variability, as demonstrated in Sec. V.

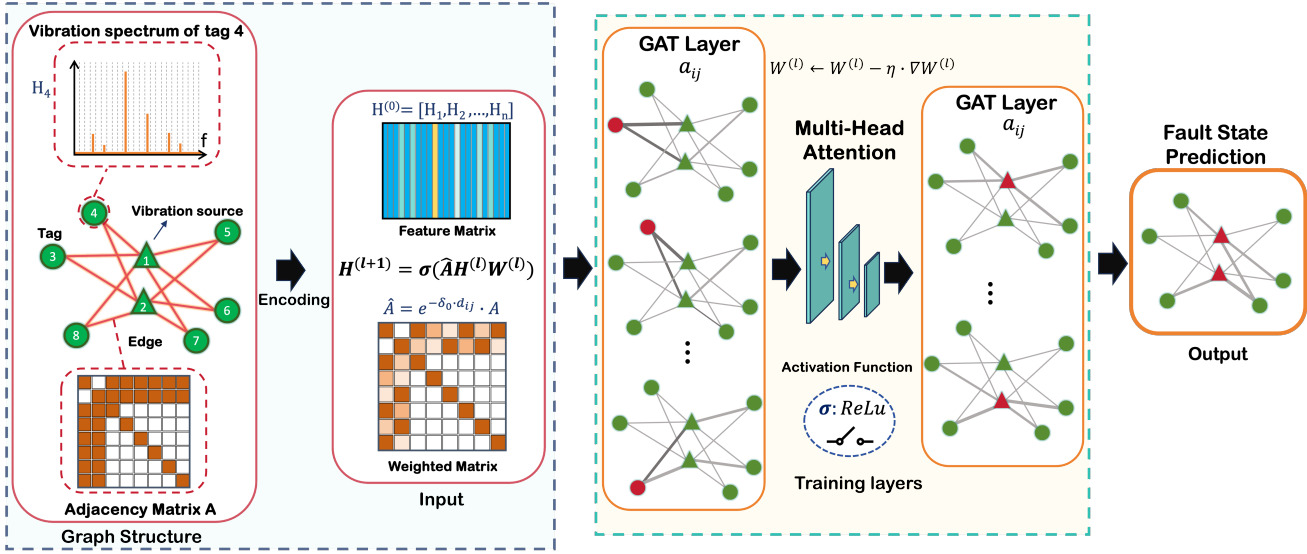


Fig. 12. Architecture of the GAT-based fault inference model. Node-level vibration features are encoded and propagated through attention-weighted graph layers. Each node aggregates information from its neighbors using learned attention coefficients α_{ij} . The GAT layer uses four parallel attention heads to capture diverse structural cues from the vibration graph. The final graph embedding is passed to a classifier to predict equipment state.



Fig. 13. Experimental setup of Vibro-Stethos. (Left) Front and back views of the custom-designed battery-free tag, integrating an RFID chip, analog JFET frontend, and a rear-mounted PZT. (Middle) Programmable vibration table with deployed tags and speaker-based excitation. (Right) Full testbed showing the tag-equipped metal plate, directional antennas, and USRP-based RFID reader.

V. IMPLEMENTATION AND EVALUATION

A. Implementation

Tag Hardware Specification: Each battery-free sensing tag uses off-the-shelf components to ensure low cost, compact form factor, and passive operation. The RFID chip (EM4325) conforms to the EPC Gen2 standard, supports selective tag activation via reader commands, and harvests RF energy for fully passive operation. An ADG902 RF switch toggles the connection between the antenna and the analog modulation circuit. The antenna is a planar PCB design, impedance-matched via an L-C network at 920 MHz. The analog frontend employs a complementary JFET pair—2SJ103 (P-channel, cutoff voltage +4 V, $R_{on} \approx 20\Omega$) and 2SK246 (N-channel, -3 V, $R_{on} \approx 25\Omega$)—which transduces PZT-induced voltage into backscatter impedance modulation. The piezoelectric transducer is mounted on the rear side of the tag and typically produces 10–1000 mV under 10–500 μm , 10–

500 Hz vibrations, while all active circuitry is located on the front. The details are summarized in Tab. II.

The tag operates fully passively by harvesting RF energy from the reader via the EM4325 chip. The complete tag measures 6 cm in diameter, 1.7 mm in thickness, and weighs 10 g. The per-unit material cost is approximately \$2.5, making it suitable for large-scale deployment.

Laboratory Testbed: We evaluate the system using a programmable vibration table mounted with a 50 cm \times 50 cm iron plate. One or two compact speakers are placed on the plate to generate vibrations via audio excitation. These signals are synthesized in MATLAB and transmitted to the speakers to emulate structural fault conditions such as imbalance, loosening, and resonance drift. Multiple tags are affixed at varying locations to capture spatially distributed vibration responses.

The RFID reader is implemented using a USRP N210, operating at 920 MHz with an output power of 18 dBm. Directional Tx and Rx antennas (20 dB gain) are positioned 3 m away

TABLE II
KEY COMPONENTS AND PARAMETERS OF THE ANALOG/RF FRONTEND.

Module	Component / Spec	Key parameters / notes
RFID IC	EM4325	EPC Gen2; passive energy harvesting; ON/OFF reference output
RF switch	ADG902	Reader-controlled tag activation path
P-JFET	2SJ103	$V_{off} \approx +4\text{ V}$; $R_{on} \approx 20\Omega$
N-JFET	2SK246	$V_{off} \approx -3\text{ V}$; $R_{on} \approx 25\Omega$
PZT transducer	VPZT	Output 10–1000 mV under 10–500 μm , 10–500 Hz vibrations
Antenna	PCB, 920 MHz	L-C matching; shared RF path for analog/digital signals

from the plate. IQ samples are collected at a sampling rate of 1 Msps and processed in real time on a MacBook Pro equipped with an Apple M2 chip and 16 GB RAM, supporting signal demodulation and offline model inference.

Experimental Illustration: Fig. 13 provides an overview of the experimental setup. The left panel shows the dual-layer sensing tag, with RFID, switch, and JFET components on the front and a PZT mounted on the rear. The center panel shows the vibration plate with multiple tags and the speaker used for excitation. The right panel depicts the complete setup, including the USRP reader and directional antennas.

Ground Truth and Baselines To ensure a rigorous evaluation, we establish a precise ground truth and compare our system against relevant baselines. Ground-truth vibration data is collected using a high-precision laser Doppler vibrometer (LDV) with an accuracy of 1 μm , positioned adjacent to each tag during experiments. In our micro-benchmark experiments, we compare *Vibro-Stethos* against mmVib [9], a state-of-the-art millimeter-wave vibration sensing system. For the fault classification task, we benchmark against a standard convolutional neural network (CNN) trained on the same spectral features under identical deployment conditions. All baselines share the same dataset and evaluation pipeline to ensure a fair comparison.

Calibration Demonstration: As the foundation for our accuracy evaluation, each tag undergoes a one-time calibration to map its normalized signal output to a physical displacement. The process is illustrated by the following example:

- 1) **Ground-Truth Measurement:** We configure the vibration table to generate a stable 50 Hz sinusoidal vibration. The LDV measures a ground-truth amplitude of $A_v = 100\text{ }\mu\text{m}$ on the surface next to the tag.
- 2) **Signal Feature Extraction:** Simultaneously, our system captures the tag's backscatter signal. After applying the path-invariant normalization procedure (detailed in Sec. IV-A), we extract a unitless, normalized amplitude feature, for which we assume a hypothetical value of $A_{norm} = 0.08$.
- 3) **Coefficient Calculation:** We then compute the calibra-

tion coefficient, C_{cal} , which maps the normalized feature to the physical displacement:

$$C_{cal} = \frac{A_v}{A_{norm}} = \frac{100\text{ }\mu\text{m}}{0.08} = 1250\text{ }\mu\text{m/unit}$$

This coefficient is then stored for this specific tag.

- 4) **Application in Measurement:** Once calibrated, if a subsequent reading from the tag yields a normalized amplitude of $A_{new} = 0.04$, the system can estimate the physical vibration as:

$$A_{estimated} = C_{cal} \times A_{new} = 1250\text{ }\mu\text{m/unit} \times 0.04 = 50\text{ }\mu\text{m}$$

This one-time calibration process effectively bridges our system's normalized signal measurements with real-world physical displacements, enabling the accurate micron-level error analysis presented in subsequent sections.

B. Vibration Measurement Accuracy

In this experiment, we evaluate the fundamental functionality of the tag, specifically assessing the measurement errors for vibration amplitude and frequency. The amplitude varies from 10 μm to 500 μm , the frequency ranges from 10Hz to 500Hz, and the distance between the tag and the vibration source ranges from 50cm to 700cm.

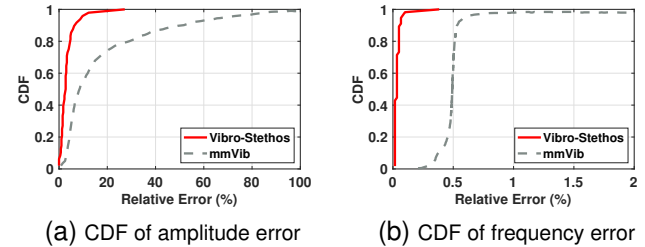


Fig. 14. Overall system performance comparison. (a) CDF of amplitude measurement error; (b) CDF of frequency measurement error. *Vibro-Stethos* consistently outperforms mmVib across all percentiles.

1) Overall Performance Summary: We begin by evaluating the end-to-end accuracy of *Vibro-Stethos* across all tested amplitude, frequency, and distance settings. Fig. 14 summarizes the cumulative distribution function (CDF) of the relative error in both amplitude and frequency, compared against mmVib [9]. As shown in Fig. 14(a), *Vibro-Stethos* achieves a median amplitude error of 2%, corresponding to a 2 μm deviation for a 100 μm vibration amplitude. This is significantly lower than mmVib, which reports a median amplitude error of 8%. Even at the 80th percentile, our system maintains an error below 4%, demonstrating stable performance across a wide range of test conditions. Similarly, Fig. 14(b) shows that *Vibro-Stethos* achieves a median frequency error below 0.1%, or 0.1 Hz at 100 Hz. In contrast, mmVib exhibits a frequency error around 0.5%, confirming the superior temporal resolution of our design. While numerically significant, these improvements also have critical practical implications for industrial diagnostics, enabling earlier fault detection and more precise fault-type identification, as detailed in the analyses below. These results validate that *Vibro-Stethos*, specifically designed to extract PZT-induced

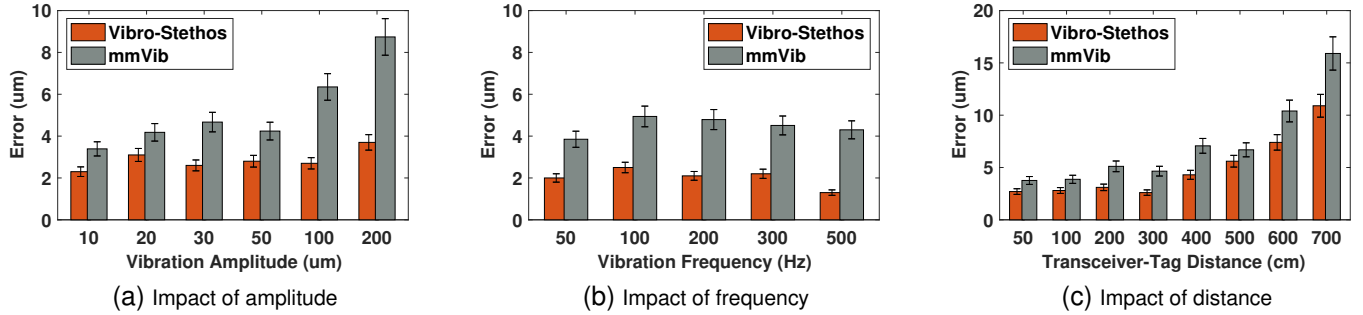


Fig. 15. Amplitude measurement error under varying conditions. (a) Impact of vibration amplitude; (b) Impact of vibration frequency; (c) Impact of tag-reader distance. *Vibro-Stethos* consistently outperforms mmVib across all scenarios.

impedance changes via passive backscatter, achieves state-of-the-art measurement accuracy in both spatial and spectral dimensions.

2) Amplitude Error Analysis: We next investigate how different factors influence amplitude measurement accuracy, including vibration amplitude, frequency, and tag-reader distance. Fig. 15 presents the comparison between *Vibro-Stethos* and mmVib across these dimensions.

Fig. 15(a) shows that as vibration amplitude increases from 10 μm to 200 μm (at 50 Hz), the absolute amplitude error of *Vibro-Stethos* remains consistently below 4 μm , with an average error of 3%. In contrast, mmVib exhibits a sharp rise in error, reaching over 8 μm at high amplitudes. This demonstrates the stability of our system's analog front-end in handling high-voltage PZT output without distortion.

Fig. 15(b) explores the effect of vibration frequency (with amplitude fixed at 100 μm). *Vibro-Stethos* maintains an average error of 2 μm across the entire 50–500 Hz range, whereas mmVib fluctuates around 4–5 μm . Both systems show limited frequency sensitivity, but our design achieves consistently lower error at all frequencies.

In Fig. 15(c), we vary the transceiver-tag distance from 50 cm to 700 cm. As expected, both systems exhibit increased error at longer distances due to reduced signal-to-noise ratio (SNR). However, the data reveals two clear benefits for *Vibro-Stethos*. First, it maintains a consistently lower absolute error across the entire range; for instance, at 300 cm, its error is approximately 40% lower than that of mmVib (3 μm vs. 5 μm). Second, *Vibro-Stethos* offers a larger effective operational range. If we define a practical error ceiling of 5 μm for high-precision tasks, our system maintains performance below this threshold up to approximately 500 cm, whereas mmVib exceeds this limit at around 400 cm. The actual benefit, therefore, is a tangible extension of the effective operational range by approximately one meter, allowing for more flexible deployment in larger industrial spaces.

Beyond the linear distance, *Vibro-Stethos* demonstrates further practical advantages in deployment robustness compared to millimeter-wave-based systems. Millimeter-wave radar like mmVib is inherently directional and highly sensitive to the transceiver-target alignment. In contrast, as shown in our robustness tests (Fig. 17(a)), our RFID-based system is significantly less sensitive to orientation, maintaining low error

even with antenna orientation shifts of up to 45 degrees. Furthermore, our system's use of the 920 MHz UHF band offers superior penetration through common non-metallic obstacles compared to the 60 GHz signals used by mmVib. This is corroborated by our obstacle tests (Fig. 17(b)), which show negligible performance loss with materials like plastic and wood, a key advantage in cluttered industrial environments.

From a practical standpoint, the observed 2–5 μm improvement in amplitude accuracy is critical for effective predictive maintenance. Many incipient faults, such as bearing micro-cracks or initial winding looseness, begin with vibration amplitudes in the low micrometer range [37], [38], [47]. A system with an 8 μm measurement error, as observed with the baseline under high-amplitude conditions, could completely mask these early indicators. In contrast, our system's consistently lower error provides a much clearer signal, enabling the detection of faults at a much earlier stage. Furthermore, this level of precision is crucial for assessing fault severity according to industrial standards like ISO 10816 [48], [49], where small differences in amplitude can distinguish between an "acceptable" condition and one that requires immediate attention.

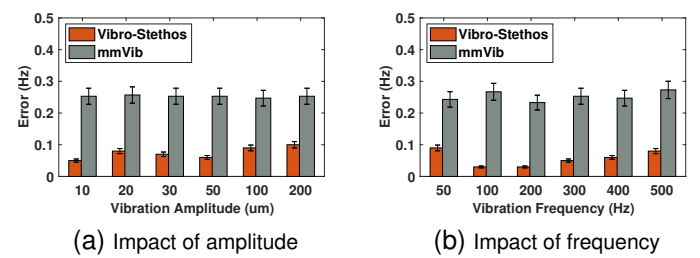


Fig. 16. Frequency estimation error under different conditions. (a) Impact of vibration amplitude; (b) Impact of vibration frequency. *Vibro-Stethos* consistently maintains sub-0.1 Hz accuracy, outperforming mmVib across all tested ranges.

3) Frequency Estimation Accuracy: We now evaluate the accuracy of frequency estimation under varying vibration amplitudes and frequencies. Fig. 16 presents the absolute frequency errors of *Vibro-Stethos* and mmVib under each condition.

In Fig. 16(a), as the amplitude increases from 10 μm to 200 μm (at a constant frequency of 100 Hz), *Vibro-Stethos* maintains an error below 0.1 Hz in all cases. In contrast,

mmVib exhibits frequency errors ranging from 0.2 Hz to 0.3 Hz. This suggests that our system is less sensitive to amplitude-induced signal quality variations.

Similarly, Fig. 16(b) shows that *Vibro-Stethos* achieves stable frequency estimation across the entire range from 50 Hz to 500 Hz, maintaining sub-0.1 Hz accuracy throughout. mmVib, on the other hand, shows increased frequency error at both low and high ends, with errors consistently exceeding 0.2 Hz.

The significance of achieving sub-0.1 Hz frequency accuracy lies in its ability to enable precise fault diagnosis. In complex machinery, different faults—such as inner versus outer race bearing failures—manifest at characteristic frequencies that may be only 1–2 Hz apart. A system with a 0.5 Hz error could easily misidentify the fault type, leading to incorrect maintenance actions. Our system's high resolution reliably distinguishes between these closely spaced spectral peaks. Moreover, it allows for the tracking of fault progression by detecting subtle frequency shifts over time, such as the change in a transformer winding's mechanical resonance, which is a key indicator of developing looseness.

These results confirm that *Vibro-Stethos* offers high-resolution frequency tracking capabilities across a wide operating range. The minimal error confirms that no significant temporal distortion occurs during the vibration-to-backscatter conversion process.

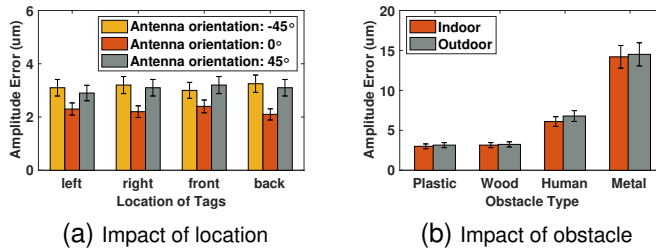


Fig. 17. Impact of deployment conditions on amplitude accuracy. (a) Effect of receiver location and antenna orientation; (b) Effect of different obstacle materials. *Vibro-Stethos* maintains low error across typical layouts, but performance degrades under strong RF obstructions.

4) Deployment Robustness Analysis: To evaluate the practical robustness of *Vibro-Stethos*, we assess its performance under variations in receiver placement, antenna orientation, and environmental obstructions. Fig. 17 summarizes the amplitude error under these conditions.

In Fig. 17(a), we place the receiver antenna in four locations relative to the vibration table—left, right, front, and back—and adjust the orientation to -45° , 0° , and $+45^\circ$ relative to the vibration plane. Results show that location changes have minimal impact on error, and orientation at 0° consistently yields the lowest error. This aligns with the directional pattern of the antenna, which is optimized for direct line-of-sight sensing.

Fig. 17(b) examines the impact of obstacles between the reader and the tag, including plastic, wood, human, and metal objects. Plastic and wood introduce negligible error increase ($< 1 \mu\text{m}$), while human bodies and metallic objects lead to more significant degradation (up to $18 \mu\text{m}$). This is expected,

as RF signals can penetrate non-conductive materials but are absorbed or reflected by lossy or conductive media.

These results indicate that *Vibro-Stethos* exhibits stable performance across typical deployment variances, but care should be taken to avoid major RF obstructions such as metal structures or human bodies in close proximity.

C. Fault Classification Performance

1) Dataset and Training Configuration: To evaluate the effectiveness of our system in classifying vibration fault states, we construct a labeled dataset comprising seven classes: one normal state (N) and six representative fault states (F1–F6), including Winding Short, Winding Loose, Winding Deformation, Insulation Shed, Core Loose, and Bearing Damage. To simulate realistic fault conditions, specific excitation signals are applied to the vibration platform to emulate the mechanical characteristics of each fault type. All labels are verified by two senior engineers from the local power utility based on the induced excitation, structural response, and domain expertise.

As illustrated in Fig. 13, eleven RFID tags are deployed on the vibration table. Six tags (green) are used for training and five (black) are reserved for testing. Each graph is constructed by randomly selecting three tags from the training set, yielding 200 unique training graphs per class. The same procedure is applied to the test tags to form 100 test graphs per class. For each graph, 10 seconds of vibration data are recorded and converted into spectral feature matrices. This process ensures both intra-class diversity and spatial layout variability across graph samples.

Table III summarizes the dataset composition, including the number of training and test graphs per class, fault descriptions, and the dominant vibration frequency bands associated with each fault type. These frequency-domain signatures are crucial for downstream spectral feature extraction and graph-based classification.

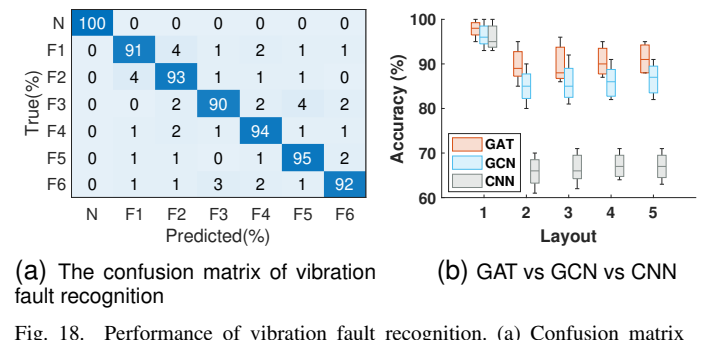


Fig. 18. Performance of vibration fault recognition. (a) Confusion matrix of 7-class classifier showing high per-class accuracy; (b) Comparison of GAT, GCN, and CNN under five tag layout distributions. GAT consistently outperforms other models, particularly under layout variability.

2) Classification Accuracy and Confusion Analysis: The confusion matrix in Fig. 18(a) presents the classification results across all seven classes. *Vibro-Stethos* achieves an overall accuracy of 93.7%. The normal class (N) is recognized with 100% accuracy due to its highly stable and distinct vibration signature. For fault types F1–F6, accuracy ranges from 90% to 95%, with minor confusion observed between acoustically

TABLE III
DATASET COMPOSITION AND FAULT CHARACTERISTICS FOR VIBRATION CLASSIFICATION

Class	Training Graphs	Test Graphs	Fault Description	Dominant Band
Normal (N)	200	100	System operates without structural anomalies; baseline reference for comparison.	—
Winding Short (F1)	200	100	Caused by inter-turn short circuit within transformer winding; leads to strong localized heating and altered vibration modes near the coil.	Mid (60–120 Hz)
Winding Loose (F2)	200	100	Caused by insufficient clamping force on windings; introduces low-frequency mechanical oscillation and inconsistent vibration responses.	Low (20–60 Hz)
Winding Deformation (F3)	200	100	Caused by electromagnetic forces or mechanical shock; distorts coil geometry and shifts natural vibration frequencies.	Mid (50–100 Hz)
Insulation Shed (F4)	200	100	Caused by insulation aging or partial discharge; results in sporadic high-frequency vibration components due to discharge pulses.	High (150–250 Hz)
Core Loose (F5)	200	100	Due to mechanical loosening of laminated core; generates continuous mid-frequency vibrations due to flux-induced rattle.	Mid (70–120 Hz)
Bearing Damage (F6)	200	100	Simulated by introducing roughness or pitting in support bearings; induces periodic high-frequency vibration peaks.	High (200–300 Hz)

similar conditions—such as F2 (Winding Loose) and F3 (Winding Deformation)—which share overlapping harmonic structures. These results validate the model's capability to distinguish subtle vibration anomalies with high fidelity.

TABLE IV
FAULT CLASSIFICATION ACCURACY (%) UNDER VARYING TAG COUNTS

Tags per Graph	1	2	3	4	5
GAT Accuracy	68.6	86.3	93.7	94.3	94.5

3) Model Generalization under Layout Shift: To assess robustness to spatial deployment variation, we compare GAT with baseline GCN and CNN models under five randomly generated tag layouts. All models are trained using layout 1 and evaluated on layouts 2–5. As shown in Fig. 18(b), the CNN model suffers significant performance degradation under layout shift, with accuracy dropping to an average of 66%. The GCN model maintains above 85% accuracy by leveraging spatial graph structures. The GAT model consistently achieves over 90% accuracy, thanks to its attention-based aggregation mechanism that dynamically prioritizes informative tag nodes, demonstrating strong generalization to deployment variability.

In practice, the tag graph is sparse (3–5 nodes) and the nodes contribute unequally: tags closer to the vibration source capture higher-SNR features that are highly discriminative, whereas peripheral tags tend to carry weaker or noisier signals. Unlike GCN, which treats all neighbors equally during aggregation, GAT adaptively assigns larger weights to the most informative nodes and downweights noisy ones. This explains why GAT consistently outperforms GCN in our experiments.

4) Impact of Tag Count on Classification Accuracy: We further examine how the number of tags per graph affects

classification performance. As shown in Table IV, the GAT model achieves 86.3% accuracy with only two tags and steadily improves as the tag count increases, reaching 94.5% with five tags. These results highlight the model's resilience to sparse input and its ability to extract meaningful vibration patterns from limited observations. In our main experiments, we use three tags per graph due to the physical constraint of the vibration platform (50 cm × 50 cm), which still offers sufficient spatial diversity for effective classification.

TABLE V
IMPACT OF MISSING TAGS ON GAT-BASED CLASSIFICATION (5-TAG DEPLOYMENT).

Condition	Macro-F1 (%)	Accuracy (%)
All 5 tags (baseline)	94.6	94.5
Missing 1 near-source tag	91.8	92.0
Missing 1 far-side tag	94.3	94.0
Missing 2 far-side tags	93.9	93.7
Missing 1 near + 1 far tag	92.7	92.4
Missing 2 near-source tags	89.5	89.0

Robustness to missing tags. In realistic deployments, individual RFID tags may become faulty or temporarily lose responses due to hardware issues or environmental blockage. To examine this effect, we conducted a stress test under a 5-tag deployment by selectively masking specific tags. As summarized in Table V, the GAT model exhibits a gradual rather than catastrophic degradation. When one far-side tag is missing, the macro-F1 remains as high as 94.3% (a drop of only 0.3 percentage points compared to the full 5-tag baseline of 94.6%). In contrast, missing a near-source tag leads to a larger but still moderate drop to 91.8%. Even in

the worst case of two near-source tags failing simultaneously, the system sustains 89.5% macro-F1. These results indicate that while tags closer to the vibration source carry more discriminative information, the attention mechanism in GAT effectively redistributes weights among the remaining nodes, ensuring robust fault classification despite partial tag failures.

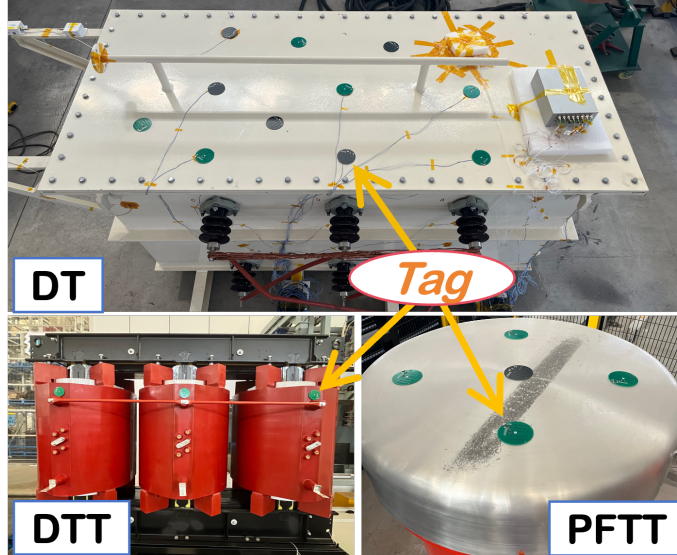


Fig. 19. Real-world deployment of *Vibro-Stethos* on three transformer types: (Top) Distribution transformer (DT), (Bottom Left) Dry-type transformer (DTT), and (Bottom Right) Power-frequency test transformer (PFTT). Tags are affixed directly to structural surfaces.

D. Real-World Deployment Case Study

To validate the practical diagnostic utility of *Vibro-Stethos* in real industrial environments, we conducted a field deployment at an operational power plant operated by Shandong Electrical Engineering & Equipment Group in Shandong, China. The site includes a variety of medium- and high-voltage transformers deployed in both indoor and outdoor settings. We selected 10 transformers spanning three representative types—distribution (DT), dry-type (DTT), and power-frequency test transformers (PFTT)—for systematic inspection. For each unit, we affixed 3 to 10 RFID sensor tags depending on the physical size and surface accessibility of the transformer. Tags were mounted near structurally significant regions such as the winding chamber, cooling fins, or chassis. An RFID reader was positioned approximately 5 m away, and data was collected wirelessly during a two-day monitoring campaign.

Among the 10 transformers inspected, the system detected abnormal vibration patterns in one unit, while the remaining nine were classified as normal. All system predictions were subsequently verified through manual inspection. To illustrate the diagnostic performance across diverse deployment scenarios, we present three representative cases: the single faulty transformer confirmed by experts, and two typical normal units with different insulation structures and installation environments. Deployment configurations for each case are shown in Fig. 19.

Case I: Distribution Transformer (DT). This outdoor transformer steps down voltage from 10 kV to 400 V. Three tags were attached near the winding chamber and cooling fins. The measured vibration frequency was 50.05 Hz—closely matching the rated grid frequency—while the amplitude was 237 μm , significantly exceeding baseline levels. The system classified this state as a winding short fault (F1) based on the harmonic response. Manual inspection confirmed this diagnosis, revealing insulation degradation and local overheating near the winding.

Case II: Dry-Type Transformer (DTT). This indoor unit supplies power to a sensitive control room and features resin-cast insulation, which naturally damps mechanical resonance. Tags were deployed on both the coil support and tank surface. The system detected a stable 50.10 Hz signal with a moderate amplitude of 56 μm . No abnormal harmonic features were observed, and the system classified this state as normal (N). Follow-up thermal and acoustic inspections corroborated the absence of fault symptoms.

Case III: Power-Frequency Test Transformer (PFTT). This lab-grade transformer is used for high-voltage testing under non-partial discharge (PD) conditions. Tags were placed symmetrically on the high-voltage bushing and chassis. The recorded vibration frequency was 49.95 Hz with an amplitude of 48 μm . The model detected no anomalies, which was consistent with the equipment's controlled and low-noise operating environment.

Summary: Table VI summarizes the vibration characteristics and validation results across all three representative units. *Vibro-Stethos* successfully detected the single faulty transformer among the 10 inspected units, and its predictions aligned with expert diagnosis. These results demonstrate the system's real-world feasibility for scalable, battery-free condition monitoring across diverse transformer architectures and deployment conditions.

E. Long-Term Deployment and Stability Validation

A critical requirement for any system aimed at preventive maintenance is the long-term stability of its measurements. To address this, we answer three key questions: (i) how is calibration performed, (ii) is it required for every tag, and (iii) does the calibration drift over time? We conducted a dedicated long-term experiment to validate our approach.

Calibration Process Our calibration strategy is a two-stage process designed for both accuracy and scalability.

- Batch Consistency:** The PZT sensors are screened at the factory to ensure high consistency of their core piezoelectric properties (d_{33} and C_{PZT}) across a batch. This provides a uniform baseline response.
- One-Time On-site Calibration:** To account for installation-specific variables (e.g., mounting pressure, surface coupling) that affect the final effective mapping coefficient, a one-time, on-site calibration is performed for each tag upon deployment. As detailed in the example in Sec. V-A, this procedure uses a portable LDV to establish a precise, individualized mapping function for the tag in its final mounted position. This calibration does not need to be repeated.

TABLE VI

SUMMARY OF REAL-WORLD DEPLOYMENTS ON THREE TRANSFORMER TYPES (AMONG 10 TRANSFORMERS TESTED, 3 ARE REPORTED BELOW AS REPRESENTATIVE CASES).

Transformer Type	Rated Freq (Hz)	Measured Freq (Hz)	Amplitude (μm)	State	Inference	Manual Inspection
Distribution (DT)	50.00	50.05	237	Abnormal	Winding Short (F1)	Insulation Degradation
Dry-Type (DTT)	50.00	50.10	56	Normal	Normal	No Issue
PFTT (Lab)	50.00	49.95	48	Normal	Normal	No Issue

Long-Term Stability Experiment To empirically validate the stability of this one-time calibration, we conducted a three-month monitoring campaign at the Shandong Electrical Engineering & Equipment Group facility. We deployed 10 Vibro-Stethos tags on an operational 10 kV dry-type transformer. The transformer's inherent 50 Hz vibration, caused by magnetostriction from the grid's line frequency, served as a stable and persistent reference signal. We performed an initial calibration for all 10 tags at the start of the deployment (Month 0) and re-evaluated their measurements after three months (Month 3).

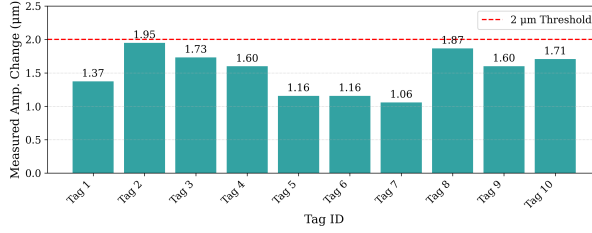


Fig. 20. Long-term calibration stability over a three-month deployment. The bars show the drift in the measured amplitude of a stable 50 Hz reference vibration for 10 tags. The drift for all tags is less than 2 μm , demonstrating the high reliability of the one-time calibration process.

The results are presented in Fig. 20. The figure shows the change in the measured amplitude of the stable 50 Hz reference signal for each of the 10 tags over the three-month period. The drift is remarkably low; for all 10 tags, the change in the measured amplitude was less than 2 μm . This result strongly validates that our one-time calibration is robust and that the sensor's mapping coefficient exhibits negligible drift over several months of continuous operation. This level of stability is crucial and demonstrates the system's suitability for long-term industrial fault diagnosis and preventive maintenance.

It is worth noting that the measured 2 μm calibration error is minor compared to the vibration magnitudes in our target industrial scenarios. Transformer steady-state vibrations range from tens to hundreds of micrometers, and fault signals typically exceed 20–50 μm [48], [49]. Therefore, a 2 μm deviation (< 5–10% relative error) is sufficiently small for detecting most practical anomalies. While the relative error reaches 20% at the 10 μm level, we define our system's scope as targeting these larger, practical industrial fault signals. Detecting sub-10 μm vibrations, which would require specialized instruments like LDVs [5] (used as ground-truth in our own validation), is explicitly beyond our target application. Most importantly, this offset (arising from mounting tolerance

and material drift) remains **stable** over time. For long-term predictive maintenance, the goal is tracking the vibration **trend**. A stable offset does not impact this trend analysis, and its long-term influence is therefore negligible.

VI. DISCUSSION

We now reflect on practical design trade-offs, system limitations, and real-world deployment challenges associated with *Vibro-Stethos*. This discussion is informed by both laboratory evaluations and field deployments across industrial transformer environments.

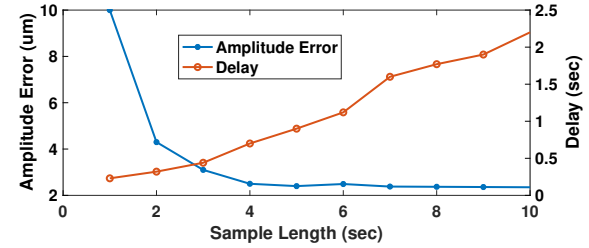


Fig. 21. Tradeoff between amplitude measurement error and detection delay with varying sample length.

A. Practical System Considerations

Tradeoff Between Sampling Duration and Responsiveness: In industrial applications, vibration detection systems must balance accuracy with real-time responsiveness. To analyze this tradeoff, we varied the sampling duration from 1 s to 10 s at a fixed tag sampling rate of 1 Msps. As shown in Fig. 21, amplitude error decreases with longer durations due to improved spectral resolution, stabilizing below 2.5 μm after 4 s. However, delay increases linearly with window size, reaching 2.2 s at 10 s. Based on this tradeoff, we recommend a 4 s sampling window as a practical operating point, offering a good balance between spectral fidelity and latency.

B. Design Choice Justification

Our design adopts a complementary dual-JFET frontend rather than other analog options. Enhancement-mode MOS-FETs, while common in switching circuits, require biasing or charge pumps to conduct, which is infeasible in a battery-free tag. JFETs, by contrast, operate with near-zero gate current and respond directly to the millivolt-level output of the PZT. Diode-based clippers also perform poorly because their forward thresholds (0.2–0.7 V) are comparable to or higher than the PZT output range (10–1000 mV). In series form, sub-threshold signals cannot pass; in shunt form, near-threshold

TABLE VII
RECOMMENDED DEPLOYMENT AND ANALYSIS STRATEGIES FOR DIFFERENT INDUSTRIAL EQUIPMENT

Equipment Type	Vibration Characteristics	Tag Count	Recommended Sampling Strategy	Recommended Analysis Method
Power Transformer [38]	Stable, periodic; complex spatial fault patterns.	Multi-tag (3–10)	Slow Sequential Polling (e.g., 10s window/tag for high frequency resolution).	Frequency-Domain + GAT Model
Rotating Machinery [40] (Motors, Pumps)	Steady-state, periodic; localized fault signatures (e.g., at bearings).	Few-tag (1–3)	Key-Point Polling (e.g., 3s window/tag) for steady-state monitoring.	Frequency-Domain (FFT)
Impact-Based Machinery [50] (Stamping Presses)	Transient, non-periodic; short-duration, high-energy impacts.	Single-tag (1)	Continuous Monitoring (No polling) to eliminate monitoring blind spots.	Time-Domain (e.g., STFT, Peak Detection)

signals are flattened, destroying amplitude fidelity. Differential amplifiers, although capable of full-wave recovery, require active biasing and external power, conflicting with passive and low-cost design constraints. In contrast, the dual-JFET configuration enables passive, bidirectional impedance modulation with comparable on-resistances, achieving accurate full-wave restoration while preserving antenna compatibility and ensuring robust vibration sensing.

C. Deployment Strategies for Diverse Industrial Equipment

The reviewer's comment regarding the stability of industrial vibrations is insightful, as a single monitoring strategy is not optimal for all types of machinery. The ideal deployment of *Vibro-Stethos* depends on the spatiotemporal characteristics of the equipment's vibration. We categorize the application scenarios into two main types:

1) *Spatially-Complex and Stable Systems*: This category includes our primary target: large power transformers (DT, DTT, PFTT). These systems are characterized by:

- **Spatial Complexity**: Their large size and complex internal structures mean that faults often manifest as subtle, spatially distributed vibration patterns. A single sensor is often insufficient for a reliable diagnosis.
- **Temporal Stability**: Their vibration state, primarily driven by the stable grid frequency, remains consistent over several minutes.

For this category, our proposed method of using **multi-tag fusion with sequential polling** is the optimal strategy. The GAT model is specifically designed to interpret these complex spatial patterns. The polling period (e.g., 50 seconds for five tags) is well within the window of temporal stability, validating our quasi-synchronous data fusion approach.

2) *Systems with Transient Vibration Events*: This category includes machinery where short-lived, transient events are critical indicators, such as impact-based machines or rotating machinery during sudden load changes.

- **The Key Challenge**: The primary challenge for these systems is not the data volume per sample—our 1 Msps sampling rate is sufficient to capture the details of any

transient waveform in the time domain. The true bottleneck is the **monitoring blind spots** created by the sequential polling mechanism. For instance, in a 3-tag, 30-second polling cycle, each tag is dormant for 20 seconds, potentially missing a transient event entirely.

To address this, two alternative strategies can be employed:

- 1) **Single-Tag Continuous Monitoring**: For applications focused on event *detection* at a critical location, a single tag can be monitored continuously, eliminating all blind spots. The analysis would then shift from the FFT-based methods used in this paper to **time-domain analysis** (e.g., energy spike detection or STFT) to identify and characterize transient events. This sacrifices spatial information for 100% temporal coverage.
- 2) **Fast Polling**: For applications requiring both some spatial coverage and faster response, the per-tag sampling window can be shortened (e.g., to 1 second). This reduces the total polling cycle time, thereby reducing the duration of blind spots and increasing the *probability* of capturing a random transient event. However, this comes at the cost of a significant reduction in frequency resolution, a key advantage of our system for high-precision diagnostics.

To provide a clear guide for applying *Vibro-Stethos* to different scenarios, we summarize the recommended deployment and analysis strategies in Table VII. The table underscores a key principle: the optimal strategy is dictated by the equipment's characteristic vibration. For large, stable equipment like power transformers, where fault signatures can be spatially complex, the full multi-tag, GAT-based fusion approach with slow polling is ideal. In contrast, for rotating machinery with more localized fault signatures, a focused deployment with fewer tags is often sufficient. For equipment dominated by short-lived transient events, the strategy must shift from sequential polling to continuous single-tag monitoring to eliminate monitoring blind spots, which in turn requires a move from frequency-domain to time-domain analysis.

VII. CONCLUSION

We presented *Vibro-Stethos*, a fully battery-free sensing system for accurate micron-level vibration monitoring and fault classification in industrial environments. By integrating a dual-JFET analog modulation circuit with RFID backscatter and a GAT-based inference model, the system enables real-time, passive detection of structural anomalies. Extensive evaluation demonstrates 2 μm amplitude accuracy and robust classification across varying tag layouts. Real-world deployment on three transformer types confirms the system's practicality and diagnostic value. *Vibro-Stethos* offers a scalable, maintenance-free solution for long-term equipment health monitoring and lays the foundation for broader applications in passive industrial sensing.

REFERENCES

- [1] S. Xu, F. Xing, R. Wang, W. Li, Y. Wang, and X. Wang, "Vibration sensor for the health monitoring of the large rotating machinery: Review and outlook," *Sensor Review*, vol. 38, no. 1, pp. 44–64, 2018.
- [2] Z. Ghemari, S. Belkhiri, M. R. Morakchi, and S. Saad, "Enhancing the piezoelectric accelerometer for effective monitoring and diagnosis of engineering structures," *Romanian Journal of Acoustics and Vibration*, vol. 21, no. 1, pp. 12–19, 2024.
- [3] Z. Gong, L. Han, Z. An, L. Yang, S. Ding, and Y. Xiang, "Empowering smart buildings with self-sensing concrete for structural health monitoring," in *Proceedings of the ACM SIGCOMM 2022 Conference*, 2022, pp. 560–575.
- [4] F. L. M. dos Santos, B. Peeters, J. Lau, W. Desmet, and L. C. S. Goes, "The use of strain gauges in vibration-based damage detection," in *Journal of Physics: conference series*, vol. 628, no. 1. IOP Publishing, 2015, p. 012119.
- [5] L. Scalise, Y. Yu, G. Giuliani, G. Plantier, and T. Bosch, "Self-mixing laser diode velocimetry: application to vibration and velocity measurement," *IEEE Transactions on instrumentation and measurement*, vol. 53, no. 1, pp. 223–232, 2004.
- [6] P. Castellini, M. Martarelli, and E. P. Tomasini, "Laser doppler vibrometry: Development of advanced solutions answering to technology's needs," *Mechanical systems and signal processing*, vol. 20, no. 6, pp. 1265–1285, 2006.
- [7] L. Yang, Y. Li, Q. Lin, H. Jia, X.-Y. Li, and Y. Liu, "Tagbeat: Sensing mechanical vibration period with cots rfid systems," *IEEE/ACM transactions on networking*, vol. 25, no. 6, pp. 3823–3835, 2017.
- [8] Y. Feng, Y. Zhang, P. Yang, H. Zhou, H. Du, and X.-Y. Li, "Rf-ear ++: A mechanical identification and troubleshooting system based on contactless vibration sensing," *IEEE Transactions on Mobile Computing*, vol. 22, no. 12, pp. 7310–7326, 2022.
- [9] C. Jiang, J. Guo, Y. He, M. Jin, S. Li, and Y. Liu, "mmvib: micrometer-level vibration measurement with mmwave radar," in *Proceedings of the 26th Annual International Conference on Mobile Computing and Networking*, 2020, pp. 1–13.
- [10] Y. Yang, H. Xu, Q. Chen, J. Cao, and Y. Wang, "Multi-vib: Precise multi-point vibration monitoring using mmwave radar," *Proceedings of the ACM on Interactive, Mobile, Wearable and Ubiquitous Technologies*, vol. 6, no. 4, pp. 1–26, 2023.
- [11] J. Guo, Y. He, C. Jiang, M. Jin, S. Li, J. Zhang, R. Xi, and Y. Liu, "Measuring micrometer-level vibrations with mmwave radar," *IEEE Transactions on Mobile Computing*, vol. 22, no. 4, pp. 2248–2261, 2021.
- [12] Y. Feng, D. Dai, X. Zhao, J. Tong, Z. Gong, and L. Yang, "Deciphering micro-scale, sub-hertz mechanical vibrations in industry 4.0: A battery-free sensing approach," in *2025 IEEE International Conference on Pervasive Computing and Communications (PerCom)*. IEEE Computer Society, 2025, pp. 222–228.
- [13] S. Akiyama, M. Yoshida, Y. Moriyama, H. Suwa, and K. Yasumoto, "Estimation of walking direction with vibration sensor based on piezoelectric device," in *2020 IEEE International Conference on Pervasive Computing and Communications Workshops (PerCom Workshops)*. IEEE, 2020, pp. 1–6.
- [14] J. Liu, C. Wang, Y. Chen, and N. Saxena, "Vibwrite: Towards finger-input authentication on ubiquitous surfaces via physical vibration," in *Proceedings of the 2017 ACM SIGSAC Conference on Computer and Communications Security*, 2017, pp. 73–87.
- [15] R. Binali, H. Demirpolat, M. Kuntoğlu, M. Makhesana, S. Yaghoubi, and B. Sayın Kul, "A comprehensive review on low-cost mems accelerometers for vibration measurement: Types, novel designs, performance evaluation, and applications," *Journal of Molecular & Engineering Materials*, vol. 12, no. 3, 2024.
- [16] M. Zhao, Y. Qi, H. Wang, Z. Xie, B. Li, H. Wang, and X. Wei, "Optical interferometric mems accelerometers," *Laser & Photonics Reviews*, vol. 18, no. 2, p. 2300713, 2024.
- [17] Z. Sheng, B. Chen, W. Hu, K. Yan, H. Miao, Q. Zhang, Q. Yu, and Y. Fu, "Ldv-induced stroboscopic digital image correlation for high spatial resolution vibration measurement," *Optics Express*, vol. 29, no. 18, pp. 28 134–28 147, 2021.
- [18] J. G. Chen, A. Davis, N. Wadhwa, F. Durand, W. T. Freeman, and O. Büyüköztürk, "Video camera-based vibration measurement for civil infrastructure applications," *Journal of Infrastructure Systems*, vol. 23, no. 3, p. B4016013, 2017.
- [19] Q. Zhu, D. Cui, Q. Zhang, and Y. Du, "A robust structural vibration recognition system based on computer vision," *Journal of Sound and Vibration*, vol. 541, p. 117321, 2022.
- [20] Y. Zhang, G. Laput, and C. Harrison, "Vibrosight: Long-range vibrometry for smart environment sensing," in *Proceedings of the 31st Annual ACM Symposium on User Interface Software and Technology*, 2018, pp. 225–236.
- [21] F. Tonolini and F. Adib, "Networking across boundaries: enabling wireless communication through the water-air interface," in *Proceedings of the 2018 Conference of the ACM Special Interest Group on Data Communication*, 2018, pp. 117–131.
- [22] K. Ali and A. X. Liu, "Fine-grained vibration based sensing using a smartphone," *IEEE Transactions on Mobile Computing*, vol. 21, no. 11, pp. 3971–3985, 2021.
- [23] P. Li, Z. An, L. Yang, P. Yang, and Q. Lin, "Rfid harmonic for vibration sensing," *IEEE Transactions on Mobile Computing*, vol. 20, no. 4, pp. 1614–1626, 2019.
- [24] Y. Yang, G. Wang, Z. An, G. Zhang, X. Cheng, and P. Hu, "Rf-parrot: Wireless eavesdropping on wired audio," in *IEEE INFOCOM 2024-IEEE Conference on Computer Communications*. IEEE, 2024, pp. 701–710.
- [25] Z. Chen, T. Zheng, C. Cai, Y. Gao, P. Hu, and J. Luo, "Wider is better? contact-free vibration sensing via different cots-rf technologies," in *IEEE INFOCOM 2023-IEEE Conference on Computer Communications*. IEEE, 2023, pp. 1–10.
- [26] Y. Zheng, Y. He, M. Jin, X. Zheng, and Y. Liu, "Red: Rfid-based eccentricity detection for high-speed rotating machinery," in *IEEE INFOCOM 2018-IEEE Conference on Computer Communications*. IEEE, 2018, pp. 1565–1573.
- [27] B. Xie, J. Xiong, X. Chen, and D. Fang, "Exploring commodity rfid for contactless sub-millimeter vibration sensing," in *Proceedings of the 18th Conference on Embedded Networked Sensor Systems*, 2020, pp. 15–27.
- [28] P. Caldero and D. Zeeke, "Multi-channel real-time condition monitoring system based on wideband vibration analysis of motor shafts using saw rfid tags coupled with sensors," *Sensors*, vol. 19, no. 24, p. 5398, 2019.
- [29] V. Ranganathan, S. Gupta, J. Lester, J. R. Smith, and D. Tan, "Rf bandaid: A fully-analog and passive wireless interface for wearable sensors," *Proceedings of the ACM on Interactive, Mobile, Wearable and Ubiquitous Technologies*, vol. 2, no. 2, pp. 1–21, 2018.
- [30] N. Arora, A. Mirzaadeh, I. Moon, C. Ramey, Y. Zhao, D. C. Rodriguez, G. D. Abowd, and T. Starner, "Mars: Nano-power battery-free wireless interfaces for touch, swipe and speech input," in *The 34th Annual ACM Symposium on User Interface Software and Technology*, 2021, pp. 1305–1325.
- [31] W. Li, R. Spolaor, C. Luo, Y. Sun, H. Chen, G. Zhang, Y. Yang, X. Cheng, and P. Hu, "Acoustic eavesdropping from sound-induced vibrations with multi-antenna mmwave radar," *IEEE Transactions on Mobile Computing*, 2025.
- [32] C. Lin, C. Ji, J. Xiong, C. Xiang, L. Wang, G. Wu, and Q. Zhang, "Wirotate: An instantaneous angular speed measurement system using wifi signals," *IEEE Transactions on Mobile Computing*, vol. 23, no. 1, pp. 985–1000, 2022.
- [33] S. Jian, S. Ishida, and Y. Arakawa, "Initial attempt on wi-fi csi based vibration sensing for factory equipment fault detection," in *Adjunct proceedings of the 2021 international conference on distributed computing and networking*, 2021, pp. 163–168.
- [34] C. Wang, F. Lin, T. Liu, K. Zheng, Z. Wang, Z. Li, M.-C. Huang, W. Xu, and K. Ren, "Inmeve: eavesdropping on smartphone's earpiece via cots mmwave device," in *Proceedings of the 28th Annual International Conference on Mobile Computing And Networking*, 2022, pp. 338–351.

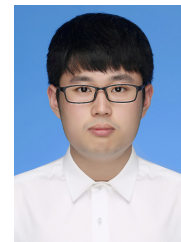
- [35] C. Wang, F. Lin, H. Yan, T. Wu, W. Xu, and K. Ren, “{VibSpeech}: Exploring practical wideband eavesdropping via bandlimited signal of vibration-based side channel,” in *33rd USENIX Security Symposium (USENIX Security 24)*, 2024, pp. 3997–4014.
- [36] Z. Zhang, L. Lombardo, T. Shi, X. Han, M. Parvis, and J. Li, “A smart combined wireless sensor network for vibration and ae signals measurement,” *IEEE Transactions on Instrumentation and Measurement*, 2025.
- [37] X. Duan, T. Zhao, J. Liu, L. Zhang, and L. Zou, “Analysis of winding vibration characteristics of power transformers based on the finite-element method,” *Energies*, vol. 11, no. 9, p. 2404, 2018.
- [38] K. Hong, M. Jin, and H. Huang, “Transformer winding fault diagnosis using vibration image and deep learning,” *IEEE Transactions on Power Delivery*, vol. 36, no. 2, pp. 676–685, 2020.
- [39] J. Pacheco-Chérrez, J. A. Fortoul-Díaz, F. Cortés-Santacruz, L. M. Aloso-Valerdi, and D. I. Ibarra-Zarate, “Bearing fault detection with vibration and acoustic signals: Comparison among different machine leaning classification methods,” *Engineering Failure Analysis*, vol. 139, p. 106515, 2022.
- [40] T. Chu, T. Nguyen, H. Yoo, and J. Wang, “A review of vibration analysis and its applications,” *Heliyon*, vol. 10, no. 5, 2024.
- [41] P. Huang, Y. Wang, Y. Gu, and G. Qiu, “A bearing rul prediction approach of vibration fault signal denoise modeling with gate-cnn and conv-transformer encoder,” *Measurement Science and Technology*, vol. 35, no. 6, p. 066104, 2024.
- [42] P. Velickovic, G. Cucurull, A. Casanova, A. Romero, P. Lio, Y. Bengio et al., “Graph attention networks,” *stat*, vol. 1050, no. 20, pp. 10–48 550, 2017.
- [43] A. Sedra, K. Smith, T. C. Carusone, and V. Gaudet, “Microelectronic circuits 8th edition,” *Chapter*, vol. 14, pp. 1235–1236, 2020.
- [44] EM Microelectronic, “Em4325 uhf rfid ic product page,” <https://www.emmicroelectronic.com/product/epc-and-uhf-ics/em4325>, 2025, accessed: 2025-06-04.
- [45] C. A. Balanis, *Antenna Theory: Analysis and Design*, 4th ed. John Wiley & Sons, 2016.
- [46] T. N. Kipf and M. Welling, “Semi-supervised classification with graph convolutional networks,” *arXiv preprint arXiv:1609.02907*, 2017.
- [47] S. Meziani, D. Zarour, and M. Thomas, “Experimental study for early detection of bearing defects by vibration and acoustic emission,” in *CFM 2017-23ème Congrès Français de Mécanique*. AFM, Maison de la Mécanique, 39/41 rue Louis Blanc-92400 Courbevoie, 2017.
- [48] I. Standard, “Mechanical vibration-evaluation of machine vibration by measurements on non-rotating parts,” *ISO/IS*, vol. 10816, 1996.
- [49] ISO 20816-1:2016 *Mechanical vibration — Measurement and evaluation of machine vibration*, International Organization for Standardization Std., 2016, reaffirmed 2014.
- [50] Y.-J. Chang, L.-J. Chen, Y. Tu, H.-P. Yang, and C.-K. Lee, “Building the health monitoring and fault diagnosis models for stamping press,” in *PHM Society Asia-Pacific Conference*, vol. 4, no. 1, 2023.



Yuanhao Feng received the B.S. degree from the College of Computer Science and Technology, Northeastern University, China, in 2017. He obtained the Ph.D. degree in Computer Science and Technology from the University of Science and Technology of China in 2023. He is currently a Postdoctoral Researcher at The Hong Kong Polytechnic University. His research interests include wireless sensing, embodied intelligence, and intelligent systems.



Donghui Dai received the B.E. degree from the School of Electronics and Information Technology at Sun Yat-sen University, China, in 2020. He obtained his Ph.D. degree from the Department of Computing at The Hong Kong Polytechnic University in 2025 and is currently an Assistant Professor (Research) in the same department. His research interests include backscatter communication, wireless security, and mobile computing.



Jinyang Huang is a lecturer at the School of Computer Science and Information Engineering, Hefei University of Technology and the Secretary-General of the Anhui Province Key Laboratory of Affective Computing and Advanced Intelligence Machine. He obtained his Ph.D. in Computer Science and Technology from the School of Cyberspace Security, University of Science and Technology of China in 2022. His research interests include Multimodal Perception, Human-computer Interaction, Wireless Security, and Signal Processing.



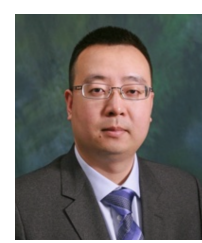
Panlong Yang (Senior Member, IEEE) received his B.S. degree, M.S. degree, and Ph.D. degree in communication and information system from Nanjing Institute of Communication Engineering, P.R. China, in 1999, 2002, and 2005 respectively. Dr. Yang is now a professor at School of Computer Science and Engineering from Nanjing University of Information Science and Technology. His research interests include wireless mesh networks, wireless sensor networks, and cognitive radio networks. He is a senior member of the IEEE Computer Society.



Xiang-Yang Li (Fellow, IEEE/ACM) is a professor and Executive Dean at School of Computer Science and Technology, USTC. He is an ACM Fellow (2019), IEEE fellow (2015), an ACM Distinguished Scientist (2014). He was a full professor at Computer Science Department of IIT. Dr. Li received MS (2000) and PhD (2001) degree at Department of Computer Science from University of Illinois Urbana-Champaign. He received a Bachelor degree at Department of Computer Science from Tsinghua University, P.R. China, in 1995. His research interests include Artificial Intelligence of Things(AIOT), privacy and security of AIOT, and data sharing and trading.



Feiyu Han received his Ph.D. degree at School of Computer Science and Technology, University of Science and Technology of China, in 2024. Before that, he received his B.S. degree at School of Computer Science and Engineering from Nanjing University of Science and Technology, in 2019. Dr. Han is working at School of Computer Science, Nanjing University of Information Science and Technology. His research interests span across wireless sensing, mobile computing, and low-power communication.



Lei Yang (Senior Member, IEEE) received the B.S. and Ph.D. degree from the School of Software and the Department of Computer Science and Technology at Xi'an Jiaotong University. He is currently working as an Associate Professor with the Department of Computing, The Hong Kong Polytechnic University. Previously, he was a postdoc fellow at the School of Software of Tsinghua University. His research interests include Internet of Things, RFID and Backscatters, Wireless and Mobile Computing.